Rare Met. (2025) 44(5):3026–3036
https://doi.org/10.1007/s12598-024-03077-x

RARE METALS

ORIGINAL ARTICLE

Antimony nanoparticles encapsulated in three-dimensional porous carbon frameworks for high-performance rechargeable batteries

An-Qi Chen, Si-Guang Guo, Yu Liu*, Ling Long, Zhuo Li*, Biao Gao, Paul K. Chu, Kai-Fu Huo

Received: 4 August 2024 / Revised: 22 August 2024 / Accepted: 23 August 2024 / Published online: 3 February 2025

Abstract Antimony (Sb) is regarded as a potential candidate for next-generation anode materials for rechargeable batteries because it has a high theoretical specific capacity, excellent conductivity and appropriate reaction potential. However, Sb-based anodes suffer from severe volume expansion of $> 135\%$ during the lithiation–delithiation process. Hence, we construct a novel Sb@C composite encapsulating the Sb nanoparticles into highly conductive three-dimensional porous carbon frameworks via the one-step magnesiothermic reduction (MR). The porous carbon provides buffer spaces to accommodate the volume expansion of Sb. Meanwhile, the three-dimensional (3D) interconnected carbon frameworks shorten the ion/electron transport pathway and inhibit the overgrowth of unstable solid-electrolyte interfaces (SEIs). Consequently, the 3D Sb@C composite displays remarkable electrochemical performance, including a high average Coulombic efficiency (CE) of $> 99\%$, high initial capability of 989 $mAh \cdot g^{-1}$, excellent cycling stability for over 1000 cycles at a high current density of 5 $A \cdot g^{-1}$. Furthermore, employing a similar approach, this 3D Sb@C design paradigm holds promise for broader applications across fast-charging and ultralong-life battery systems beyond Li^+. This work aims to advance practical applications for Sb-based anodes in next-generation batteries.

Keywords Rechargeable battery; Antimony anode; Porous carbon framework; Magnesiothermic reduction; Cycle life

An-Qi Chen and Si-Guang Guo have contributed equally to this work.

Supplementary Information The online version contains supplementary material available at https://doi.org/10.1007/s12598-024-03077-x.

A.-Q. Chen, S.-G. Guo, Y. Liu*, Z. Li*, B. Gao
The State Key Laboratory of Refractories and Metallurgy and Institute of Advanced Materials and Nanotechnology, Wuhan University of Science and Technology, Wuhan 430081, China
e-mail: liyu_lab@163.com

Z. Li
e-mail: zhuo_li@wust.edu.cn

L. Long
Hubei Huazhong Electric Power Technology Development Co., Ltd. Huazhong Electric Power Technology Building, Wuhan 430000, China

B. Gao, P. K. Chu
Department of Physics and Department of Materials Science and Engineering, City University of Hong Kong, Hong Kong 999077, China

K.-F. Huo
Wuhan National Laboratory for Optoelectronics (WNLO), Huazhong University of Science and Technology, Wuhan 430074, China

1 Introduction

Rechargeable batteries (lithium-ion batteries (LIBs) and sodium-ion batteries (SIBs)) undoubtedly play a dominant role in modern society by powering electric vehicles, smart grids and portable electronics due to their large capacity, eco-friendliness and long cycle life [1, 2]. However, the state-of-the-art graphite anodes have a small theoretical specific capacity of 372 $mAh \cdot g^{-1}$, and the commercial LIBs almost reach their theoretical density limit ($\leq$ 300 $Wh \cdot kg^{-1}$) [3]. In order to satisfy the demands for high-energy–density storage systems, developing novel electrode materials has widely stimulated extensive

research interest. Among all the candidates for anode materials, Sb-based anodes have a high theoretical capacity of 660 $mAh{\cdot}g^{-1}$ (almost 2 times the theoretical specific capacity of the graphite anode) and a low reduction potential of 0.152 V (vs. Li^+/Li) [4]. Therefore, Sb-based anodes have been regarded as prospective anode materials for high-energy–density LIBs [5]. However, Sb anodes undergo a large volume variation of > 135% during electrochemical cycling, leading to pulverization of Sb particles and subsequently resulting in rapid deterioration in the electrochemical performance.

Hybridization of Sb particles with highly conductive carbon is one of the most effective methods to address the aforementioned challenges of Sb-based anodes [6]. Notably, constructing nanodots/carbon networks composite is a valid strategy to prolong the cycle life [7, 8]. The carbonaceous materials can be used as a dispersion medium or matrix-to-hybrid with metal-based nanoparticles to prevent Sb nanoparticles from agglomerating [9]. Particularly, the Sb-C coordination compounds can buffer the large volume change of Sb nanodots and prevent solid-electrolyte interface (SEI) film damage [10]. For example, Ramireddy et al. [11] have demonstrated that embedded antimony nanoparticles can afford superior cycling stability. Although excellent lithium storage properties were obtained, the method above may result in different surface structures and inhomogeneous material, causing cycle life fugitiveness and unstable rate performance. Moreover, the ion diffusion kinetics in conventional carbon layers (e.g., amorphous carbon, graphitized carbon and hard carbon) is very sluggish, limiting the rate performance of composite materials [12]. Additionally, the synthetic procedure was cumbersome when combining the hydrothermal and annealing methods [13].

In this work, we report a feasible pathway for large-scale green preparation of a Sb-based composite anode (three-dimensional (3D) Sb@C) by encapsulating Sb nanoparticles in 3D porous carbon frameworks. The 3D Sb@C composite was synthesized via magnesiothermic reduction of $C_8H_4K_2O_{12}Sb_2$-$3H_2O$, followed by subsequent tartaric acid etching. As expected, the 3D porous carbon frameworks inlaid with Sb nanoparticles not only effectively mitigate the huge volume expansion of Sb anodes during discharge–charge processes but also shorten the ion/electron transport pathway, which accelerates the electrochemical kinetics of the energy storage. Moreover, the carbon skeleton isolates the Sb particles from the liquid electrolyte, avoiding the overgrowth of unstable SEIs. Consequently, the 3D Sb@C composite displays outstanding rate performance and excellent cycling stability in LIBs and SIBs. The Sb@C anode with low preparation cost featuring mass production as well as superior electrochemical performance promotes the commercial application of Sb for next-generation rechargeable batteries.

2 Experimental

2.1 Preparation of 3D Sb@C

1.00 g antimony potassium tartrate ($C_8H_4K_2O_{12}Sb_2$-$3H_2O$, solid, Aladdin) and 0.69 g magnesium powder (200 mesh number, Aladdin) were mixed in a mortar for about 20 min. Then, the obtained powders were transferred into a sealed stainless-steel autoclave and heated at 340 °C for 3 h to eliminate the bound water, followed by a magnesium heat reaction at 700 °C for 3 h under an Ar atmosphere. After cooling to room temperature, the 3D Sb@C product was obtained by washing with 2 wt% tartaric acid ($C_4H_4O_6$, Aladdin) solution for stirring for 4 h at 40 °C and then drying at 80 °C for 12 h in a vacuum.

2.2 Characterizations

The morphology was characterized using a scanning electron microscope (SEM, ThermoFisher Apreo S HiVac) and transmission electron microscope (TEM, FEI Titan G260-300) equipped with an X-ray energy dispersive spectrometer (EDS). The internal composition was confirmed by X-ray diffraction (XRD, Rigaku nSL9KW), Raman Spectrometer (Raman, LabRAM HR Evolution), thermogravimetry analysis (TGA) instrument (TG/DSC, Discovery SDT 650), and X-ray photoelectron spectroscopy (XPS, AXIS SUPRA+).

2.3 Electrochemical measurements

The electrode was composed of active material, acetylene black and carboxymethyl cellulose with a weight ratio of 7:1:2. The obtained mixture was further stirred with a deaeration mixer (Kurabo, KK-300SSE) for 1.5 h, then a homogeneous slurry was obtained. After being coated on the copper foil, the electrode was dried in a vacuum oven at 80 °C for 24 h and subsequently punched into circular plates with a diameter of 12 mm. The CR2032 coin-type cell was assembled in an air-filled glove box with oxygen and water content of less than 1 ppm. Celgard 2400 PE/PP/PE and glass fiber membrane were used as separators for LIBs and SIBs, respectively. Lithium and sodium metal were used as the counter electrode, respectively. 1.0 M $LiPF_6$ in ethylene carbonate (EC): diethyl carbonate (DEC) (1:1 vol%) with 10.0% fluoroethylene carbonate (FEC), and 1 M sodium hexafluorophosphate ($NaPF_6$) in 1,2-dimethoxyethane (DME) were used as the electrolytes, respectively. The electrochemical performances of half-

cells, including long-term cycling performance, rate performance and galvanostatic charge–discharge, were conducted on a Neware batteries testing system (CT-4008-5V20mA-164). An electrochemical workstation (CHI760e, Shanghai Chenhua Instrument Co., Ltd.) was utilized for cyclic voltammetry tests and electrochemical impedance spectroscopy (EIS) tests.

3 Results and discussion

3.1 Materials characterizations

The 3D Sb@C composite was obtained via embedding the nanosized Sb into carbon matrixes, as presented schematically in Fig. 1a. The 3D Sb@C composite was fabricated by simply annealing the mixture of the commercial $C_8H_4K_2O_{12}Sb_2$-$3H_2O$ and magnesium (Mg) at 700 °C for 3 h. The magnesiothermic reaction proceeds spontaneously at a reaction temperature of 450 °C. During this process, 3D porous carbon frameworks are generated in-situ induced by MgO [14]. Based on XRD and Raman analysis (Figs. S1, S2) of the sample before acid washing, the reaction process of the magnesiothermic reaction can be represented as:

$$C_8H_4K_2O_{12}Sb_2 + 8Mg = 8MgO + 8C + K_2O_2 + 2Sb + 2H_2O \quad (1)$$

After etching using a 2 wt% tartaric acid solution, the

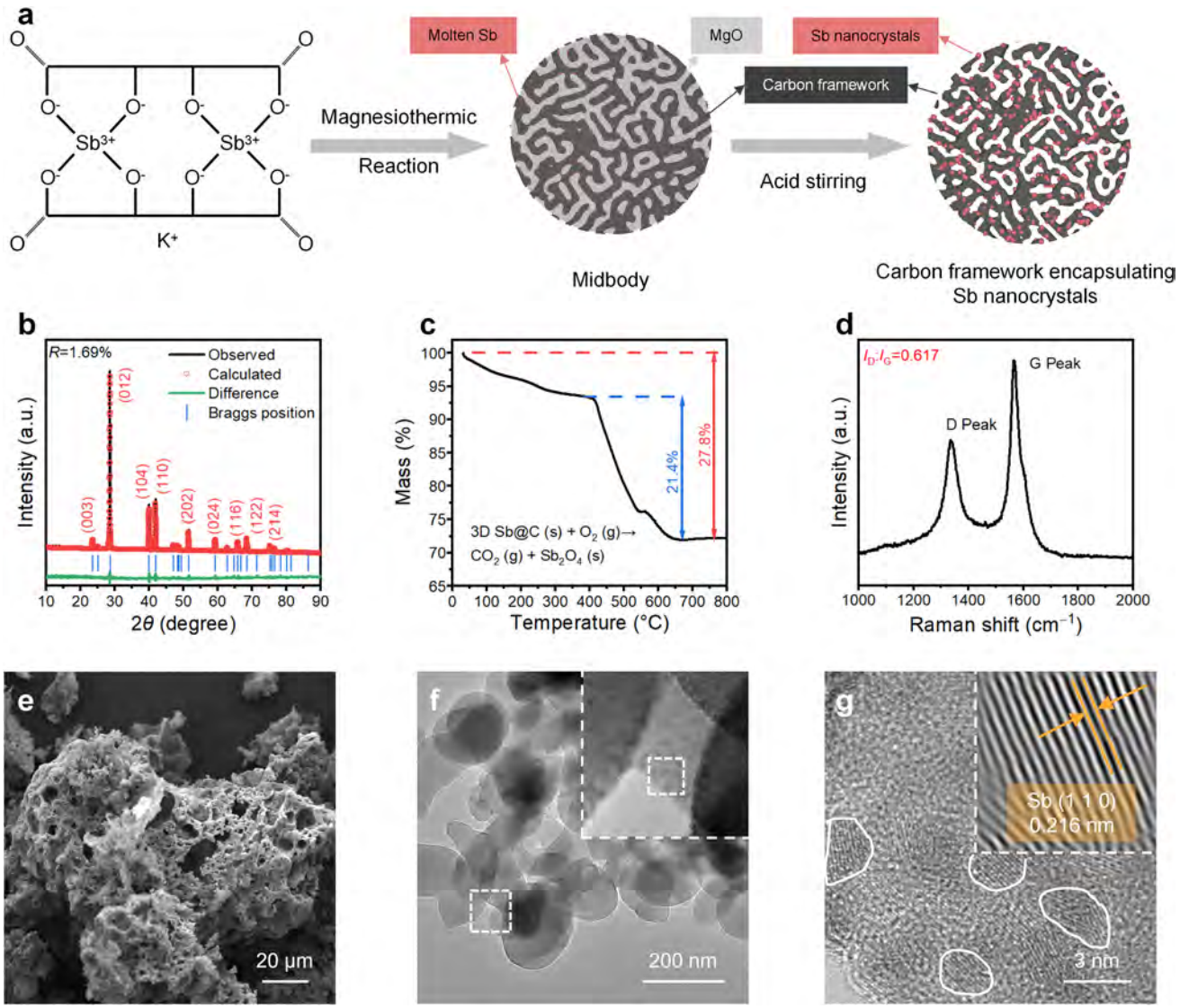

Fig. 1 Synthesis and characterization of 3D Sb@C composite. **a** Synthesis schematic diagram; **b** XRD patterns; **c** TGA profile; **d** Raman spectrum; **e** SEM image; **f** TEM and **g** HRTEM images

oxides pore former was eliminated, and the final product of a 3D carbon skeleton encapsulated with Sb nanoparticles was accomplished. In comparison to other methods, the one-step-synthetic procedure is very convenient and eco-effective. The crystallographic structures of the 3D Sb@C sample were analyzed using XRD. All diffraction peaks of the 3D Sb@C composite perfectly match with the hexagonal antimony (PDF No. 85-1322), indicating no impurities in the composite (Fig. 1b). The surface electronic states of Sb@C were characterized using XPS. As shown in Fig. S3a, XPS spectra show the strong characteristic peaks of Sb $3d_{5/2}$ at ~ 528.78 eV (Sb metal) and ~ 530.78 eV (Sb oxidization), Sb $3d_{3/2}$ at ~ 537.3 (Sb metal) and 539.58 eV (Sb oxidization). It is concluded that the surface of the Sb nanoparticles is partially oxidized, but the amount of Sb_2O_3 is quite small in these composites because no Sb_2O_3 signal was observed in XRD patterns. The C 1s profile of the Sb@C composite is deconvoluted into three peaks at 284.8, 285.9 and 287.8 eV, corresponding to the C−C, C=O and C−H bonds, respectively (Fig. S3b). From the thermogravimetric analysis of the Sb@C, the Sb content is calculated to be 72.2 wt%, while the remaining content (27.8 wt%) is assumed to be carbon (Fig. 1c) [15, 16]. According to XRD patterns, for the residue after the TG test (Fig. S4), the carbon present in the sample undergoes oxidation, producing carbon dioxide that escaped from the system. Simultaneously, monomorphic antimony undergoes transformation to eventually form Sb_2O_4 [17].

Figure 1d demonstrates the Raman spectrum of Sb@C particles. Peaks located at ~ 1350 and ~ 1550 cm^{-1} are assigned to disordered sp3-hybridised C (D-band) and graphitic sp2-hybridised C (G-band), respectively. The ratio of D and G band intensity (I_D:I_G) is 0.617, implying more defects in the carbon layers, which improves the electrical conductivity [18]. According to Brunauer–Emmett–Telle (BET) results, the pore volume is 0.134 $cm^3 \cdot g^{-1}$ with a surface area of ~ 59.79 $m^2 \cdot g^{-1}$ (Fig. S5). This unique 3D architecture enables the accommodation of volume changes in the active substance, facilitates electrolyte penetration, and shortens the ion diffusion distance. The structure of the synthesized Sb@C composite was observed using SEM. As shown in Figs. 1e, S6, S7, the 3D Sb@C composite exhibits a hollow porous structure, wherein the Sb nanoparticles are homogeneously distributed inside the carbon matrix, as confirmed by EDS mapping (Fig. S8). TEM images (Figs. 1f, S9) illustrate the nanocrystal Sb particles uniformly embedded in amorphous carbon skeletons. High-resolution TEM (HRTEM) image reveals an estimated lattice spacing of ~ 0.216 nm (Fig. 1g), corresponding to the (110) plane of Sb. EDS mapping in Fig. S10 shows that abundant Sb nanoparticles are found to be embedded in the 3D carbon matrix.

3.2 Electrochemical performance

To elucidate the mechanism for lithiation/delithiation of the 3D Sb@C electrode, CR2032-type half-cells were assembled. Cyclic voltammetry (CV) tests were performed at a scan rate of 0.1 $mV \cdot s^{-1}$ in the potential range of 0.01–2.00 V versus Li^+/Li for five cycles (Fig. 2a). During the first cathodic scan, two peaks at 1.23 and 0.57 V are clearly observed, which can be ascribed to the formation of a SEI and the alloying reaction of Sb with Li forming Li_3Sb, respectively [19]. In the subsequent cycles, only one reduction peak appears at 0.76 V, which corresponds to the multistep conversion from Sb to Li_3Sb. During the anodic scan, two oxidation reaction peaks at 1.11 and 1.43 V are attributed to two-step dealloying reactions of cubic Li_3Sb to hexagonal Li_2Sb, and Li_2Sb to rhombohedral Sb [20–23]. It is worth noting that CV curves of the second to the fifth cycle were almost overlapped, indicating the extraordinary reversibility of the 3D Sb@C electrodes.

Galvanostatic discharge–charge tests were conducted to evaluate the electrochemical performances of 3D Sb@C electrodes in LIBs, and the nano Sb was adopted as the reference electrode. Hence, the 3D Sb@C electrode delivers a first discharge capacity of 989 $mAh \cdot g^{-1}$ with a 74% initial CE and a reversible specific capacity of 593 $mAh \cdot g^{-1}$ at 0.1 $A \cdot g^{-1}$ after 200 cycles with an average CE of 99.6% (Fig. 2b, d). In contrast, the first discharge capacity of the nano Sb electrode is 686 $mAh \cdot g^{-1}$ and the reversible specific capacity is 134 $mAh \cdot g^{-1}$ at 0.1 $A \cdot g^{-1}$ after 160 cycles with an average CE of 98.2% (Fig. 2c, d). Impressively, the 3D Sb@C has better cycling stability, which is higher than the nano Sb electrode. The better cycling performance of the 3D Sb@C composite is closely related to smaller volume expansion, as expected.

The rate performance was further conducted at 0.1–5 $A \cdot g^{-1}$ (Fig. 2e, f). Obviously, the 3D Sb@C composite exhibits better rate capability with average reversible capacities of 712, 681, 631, 586, 536, 437 $mAh \cdot g^{-1}$ at 0.1, 0.2, 0.5, 1, 2, 5 $A \cdot g^{-1}$, respectively. When the current density returns to 0.2 $A \cdot g^{-1}$, the capacity is recovered to 636 $mAh \cdot g^{-1}$, 93.4% of its initial capacity, demonstrating good robustness to tolerate the current changes. In contrast, the nano Sb electrode presents a poor rate capability and only delivers reversible capacities of 606, 572, 518, 479, 434 and 361 $mAh \cdot g^{-1}$ at 0.1, 0.2, 0.5, 1, 2 and 5 $A \cdot g^{-1}$, respectively. Upon returning the current density to 0.2 $A \cdot g^{-1}$, the capacity retention of the nano Sb electrode is 86.23%. These results are mainly ascribed to the large electrode volume changes of the nano Sb during cycling. Moreover, the unique structure of Sb nanoparticles embedded in 3D porous carbon frameworks has a high specific surface area, which can improve the kinetics of the

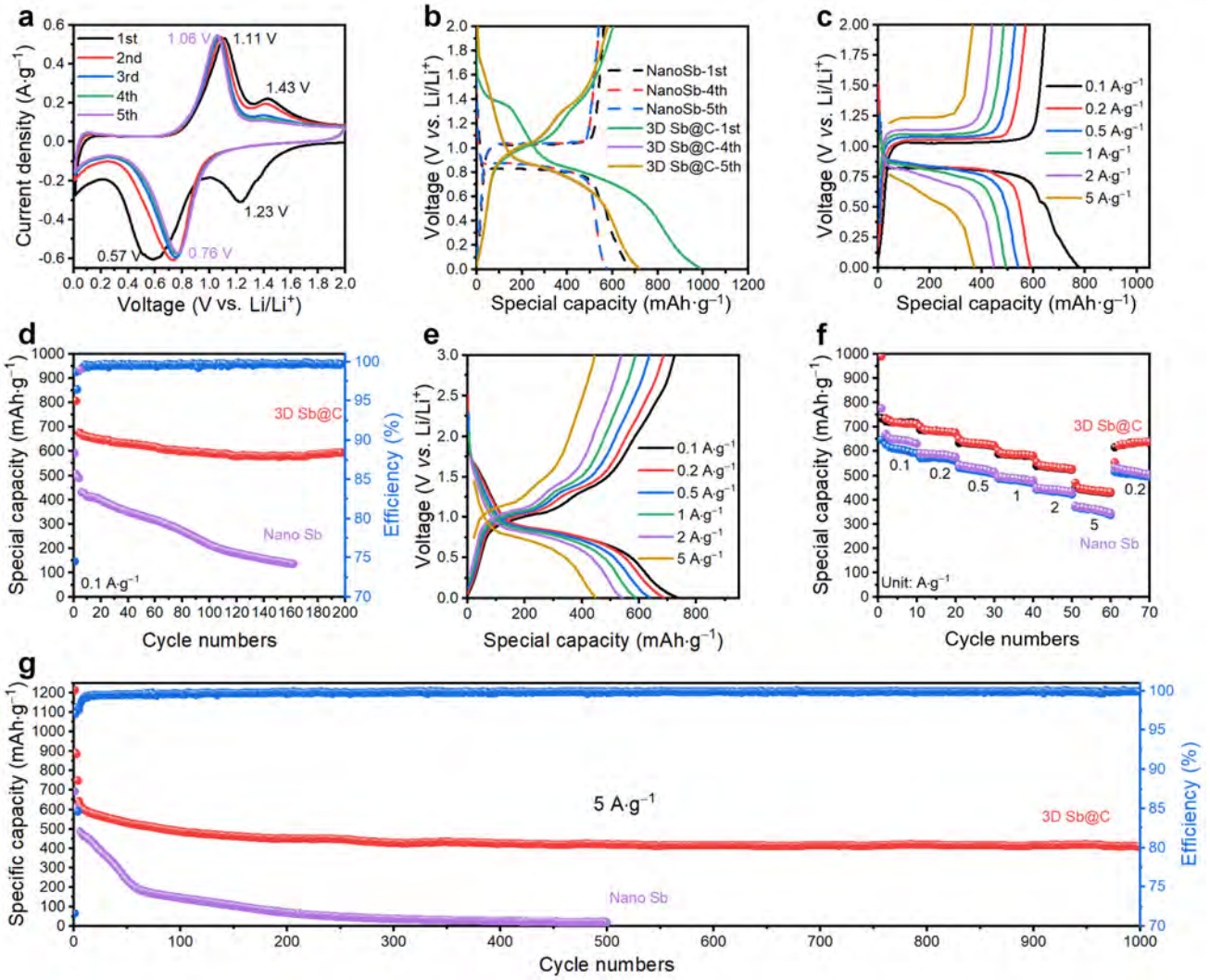

Fig. 2 Electrochemical performance of 3D Sb@C and nano Sb electrodes for LIBs. **a** CV curves at 0.1 $mV \cdot s^{-1}$ within 0.01–2.00 V; galvanostatic discharge–charge curves of **b** 3D Sb@C and nano Sb electrode at 0.1 $A \cdot g^{-1}$; **c** nano Sb electrode at different current densities and **e** 3D Sb@C electrode at different current densities; **d** cyclic stability of both electrodes at 0.1 $A \cdot g^{-1}$; **f** rate performance of both electrodes; **g** cycling performance of both electrodes at a high current of 5 $A \cdot g^{-1}$

alloying-dealloying reactions and provide plentiful void space to accommodate volume change [24].

The long-term cycling performance of both Sb electrodes at a high current density of 5 $A \cdot g^{-1}$ was also evaluated. As shown in Fig. 2g, the 3D Sb@C electrode still retains a reversible capacity of 410 $mAh \cdot g^{-1}$ after 1000 cycles with an average CE of 99.73%. In contrast, the nano Sb electrode decays quickly in capacity. These results demonstrate that the 3D Sb@C composite could serve for long-term cycling at a high C-rate because of the unique porous carbon frameworks embedded with Sb nanoparticles. To the best of our knowledge, the Li storage performance of the 3D Sb@C electrode in this study is comparable or even superior to those of other previously reported Sb@C composite anodes with a similar Sb content of approximately 68.2% ± 15% in LIBs (Fig. S11, Table S1).

The electrochemical impedance spectroscopy technique is used to analyze the operating mechanism of the 3D Sb@C electrode. The Nyquist plots of both electrodes before and after cycling are presented in Fig. 3a, b, and the equivalent circuit models are shown in Fig. S12, wherein R_{Ω}, R_{sf} and R_{ct} indicate the electrolyte resistance, SEI layer resistance and charge-transfer resistance, respectively. The fitting impedance results are summarized in Fig. 3c and Table S2. Within 100 cycles, the electrolyte resistance values of both electrodes were almost similar during cycling. The R_{sf} of the 3D Sb@C electrode slightly increases from 1.26 to 4.12 Ω, while R_{ct} decreases from 41.56 to 11.01 Ω during cycling. Although the nano Sb

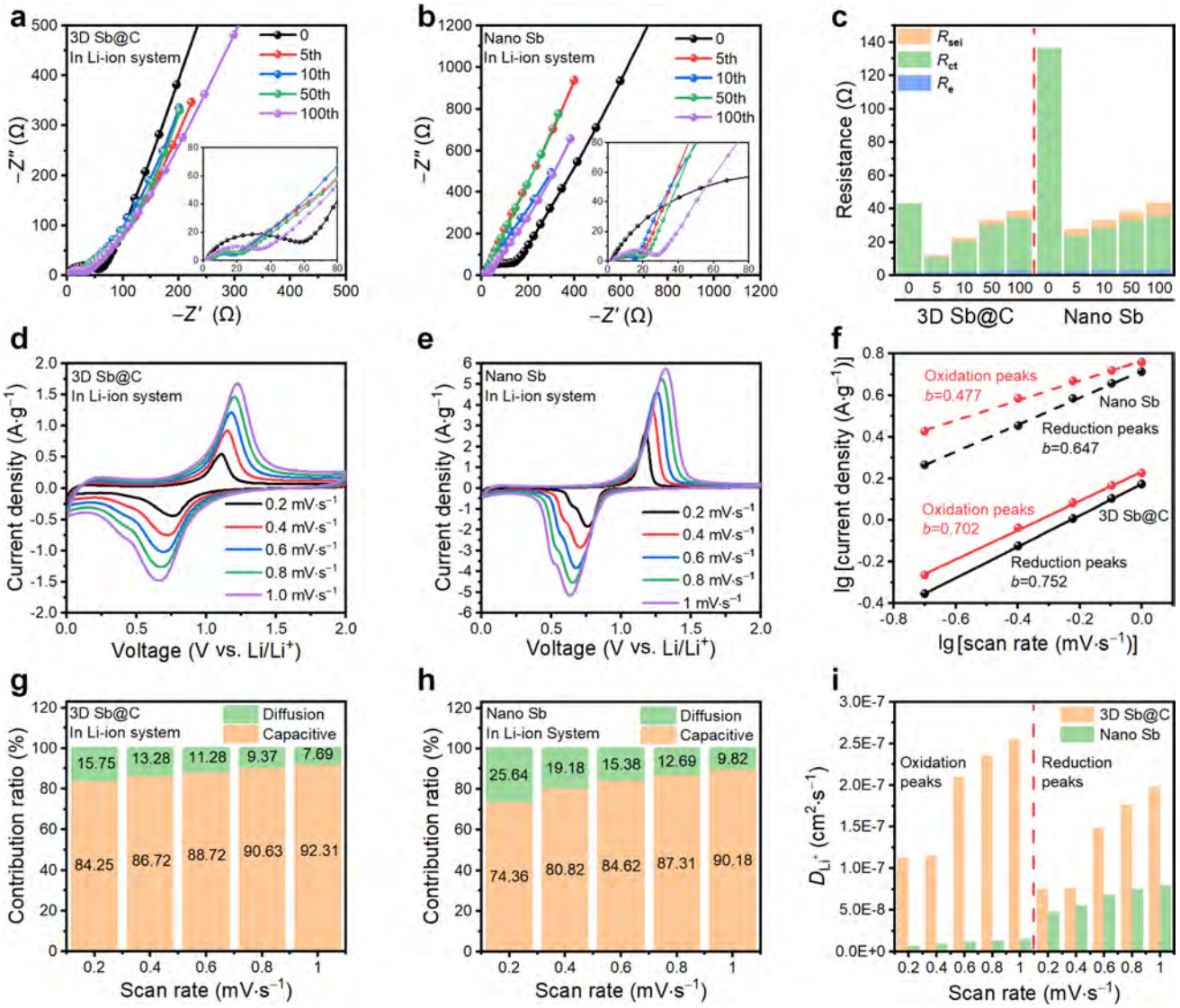

Fig. 3 Diffusion kinetic analysis of 3D Sb@C and nano Sb electrodes in LIBs. Nyquist plots of **a** 3D Sb@C and **b** nano Sb electrodes in fully charged state after different cycles at different cycles; **c** summary of calculated impedances; CV curves of **d** 3D Sb@C and **e** nano Sb electrodes at different scan rates; **f** logarithmic peak current vs. scan rate relationship; contribution ratio of diffusion-controlled and capacitance of **g** 3D Sb@C and **h** nano Sb electrodes at different scan rates; **i** Li^+ diffusion rate for 3D Sb@C and nano Sb electrodes

electrode has lower charge-transfer impedance after 5 cycles, the R_{ct} significantly increases from 21.48 Ω after 5 cycles to 31.79 Ω after 100 cycles, and the R_{sf} value increases from 3.72 to 8.16 Ω. The poor electrochemical performance is attributed to uncontrollable side-reaction between electrolyte and nano Sb electrode, the large volume change and the resultant cracking of the active material during cycling.

3.3 Diffusion kinetics

The CV was employed to analyze the kinetics of the 3D Sb@C electrode with varied scan rates in the range of 0.2–1.0 mV·s^{-1} (Fig. 3e, f). For both electrodes, the shapes of profiles at different scan rates are similar, indicating remarkable reversibility. However, the intensity of redox peaks gradually increased with the increase of scanning rate; the peak current (i) and scan rate (v) could be expressed as the following Eq. (2) [25]:

$$i = av^b \tag{2}$$

where a and b are characteristic constants for the electrochemical processes ($b = 0.5$ for diffusion-controlled behavior and $b = 1.0$ for capacitive-controlled behavior). Based on CV curves, the value of b is determined via linear fitting of Eq. (3) [26]:

$$\lg i = b\lg v + \lg a \tag{3}$$

For cathodic and anodic peaks of the 3D Sb@C and the nano Sb electrodes, the *b*-values are 0.702, 0.752 and 0.647, 0.477, respectively (Fig. 3g), suggesting that the diffusion-controlled dominates the electrochemical process for both electrodes. The contribution ratio of diffusion-controlled and capacitance-controlled can be calculated by Eq. (4) [27]:

$$i(V) = k_1 v + k_2 v^{1/2} \tag{4}$$

By dividing both sides of Eq. (3), it can be rewritten as Eq. (5) [28]:

$$i(V)\Big/_{v^{1/2}} = k_1 v^{1/2} + k_2 \tag{5}$$

Solving Eq. (5) at each potential, therefore, the diffusion-controlled current ($k_1 v^{\frac{1}{2}}$) and capacitance-controlled current ($k_2 v$) can be acquired [29], and summarized in Fig. 3h, i. For both electrodes, the capacitive effect predominates over the diffusion. The capacitance-controlled capacity of nano Sb electrode is 74.36%, 80.82%, 84.62%, 87.31% and 90.18% when the sweep speed is 0.2, 0.4, 0.6, 0.8 and 1.0 $mV{\cdot}s^{-1}$, respectively. Correspondingly, the 3D Sb@C electrode shows a capacitance contribution of 84.25%, 86.72%, 88.72%, 90.63% and 92.31% under the same sweep speed, which is more obvious than that of the nano Sb electrode. The remarkably high capacitive contribution could be related to the favorable electron transport of the 3D Sb@C composite, accelerating the electrochemical reaction kinetics.

To further investigate the kinetic advantage of 3D Sb@C composite, the Li-ion diffusion coefficient was calculated from the CV curves based following equation [30]:

$$I_p = 269000 \cdot n^{3/2} \cdot A \cdot C \cdot D^{1/2} \cdot v^{1/2} \tag{6}$$

where D is the Li-ion diffusion coefficient, which can be calculated based on the peak current (I_p), number of reaction electrons (n), electrode area (A), ionic concentration (C) and scan rate (v). The calculated Li-ion diffusion coefficients at different scan rates are summarized in Fig. 3j. Apparently, the Li-ion diffusion coefficient of the 3D Sb@C electrode is higher than that of the nano Sb electrode during lithiation–delithiation processes, revealing the faster diffusion kinetics of the 3D Sb@C composites due to the unique 3D porous carbon structure. The lithium-ion diffusion coefficients were also calculated based on EIS plots [31, 32], as presented in Fig. S13. The lithium-ion diffusion coefficient of 3D Sb@C was greater than that of Nano Sb. Notably, the lithium-ion diffusion coefficient exhibits a continuous increase with cycle number, culminating in a maximum value of 1.37×10^{-13} $cm^2{\cdot}s^{-1}$ at 10 cycles. In contrast, the diffusion coefficient of nano Sb peaked at 2.21×10^{-13} $cm^2{\cdot}s^{-1}$, an order of magnitude smaller than that of 3D Sb@C. These results are highly consistent with CV results.

3.4 Postmortem characterizations

SEM images of the 3D Sb@C, the nano Sb and the carbon skeleton without Sb particles before and after the first lithiation were evaluated to explore the morphology evolution. The 3D Sb@C electrode before lithiation appears flatter and smoother than the nano Sb and carbon skeleton without Sb electrodes, which exhibit rougher surfaces. Additionally, noticeable particles are observed on the surface of the Nano Sb electrode (Fig. S14). As shown in Fig. 4a–c, the cycled 3D Sb@C electrode shows a uniform, compact structure, and the thickness of the electrode film increases from 6.7 to 6.9 μm after lithiation, which implies good structural stability during cycling. In sharp contrast, the cycled nano Sb electrode presents obvious structural collapse and fragmentation due to the large volume expansion/contraction (Fig. 4d). Additionally, the thickness of the nano Sb electrode changes from 9.1 μm in the pristine stage to 22.1 μm in the full lithiation state after 200th cycle, corresponding to the high expansion of 142.86% (Fig. 4e, f). Notably, the surface of the porous carbon electrode maintains its initial porous structure without any cracks, and almost no thickness increase is observed (Fig. 4g–i). These results confirm that the designed porous carbon skeleton can efficiently prevent the volumetric expansion of the Sb active material during the lithiation–delithiation process, beneficial to excellent cycling and rate performances.

To better understand the reaction mechanism of the fast kinetics, in situ Raman was carried out to observe the structure evolution of the 3D Sb@C anode during cycling. As shown in Fig. 5a, b, during discharging, two broad Raman bands, corresponding to the E_g (112.4 cm^{-1}) and A_{1g} (149.3 cm^{-1}) vibration modes of crystalline Sb, become weaker, indicating the formation of Li_xSb [33]. The decrease in intensity of these characteristic peaks well supports that the Sb lithiation follows the mechanism of Sb → Li_xSb → Li_3Sb [34]. When the voltage reaches 0.01 V, a series of characteristic peaks of Li_xSb and Sb have entirely disappeared, suggesting the complete conversion from Sb to Li_3Sb. In the subsequent charge process, the characteristic peaks of Sb at 112.4 and ~ 149.3 cm^{-1} gradually recover, corresponding to the invertible delithiation process reaction from Li_xSb to Sb. However, the intensity of the Sb peaks at the end of the charging process is still significantly lower than that in the pristine electrode, demonstrating that the amorphous Sb is accumulated

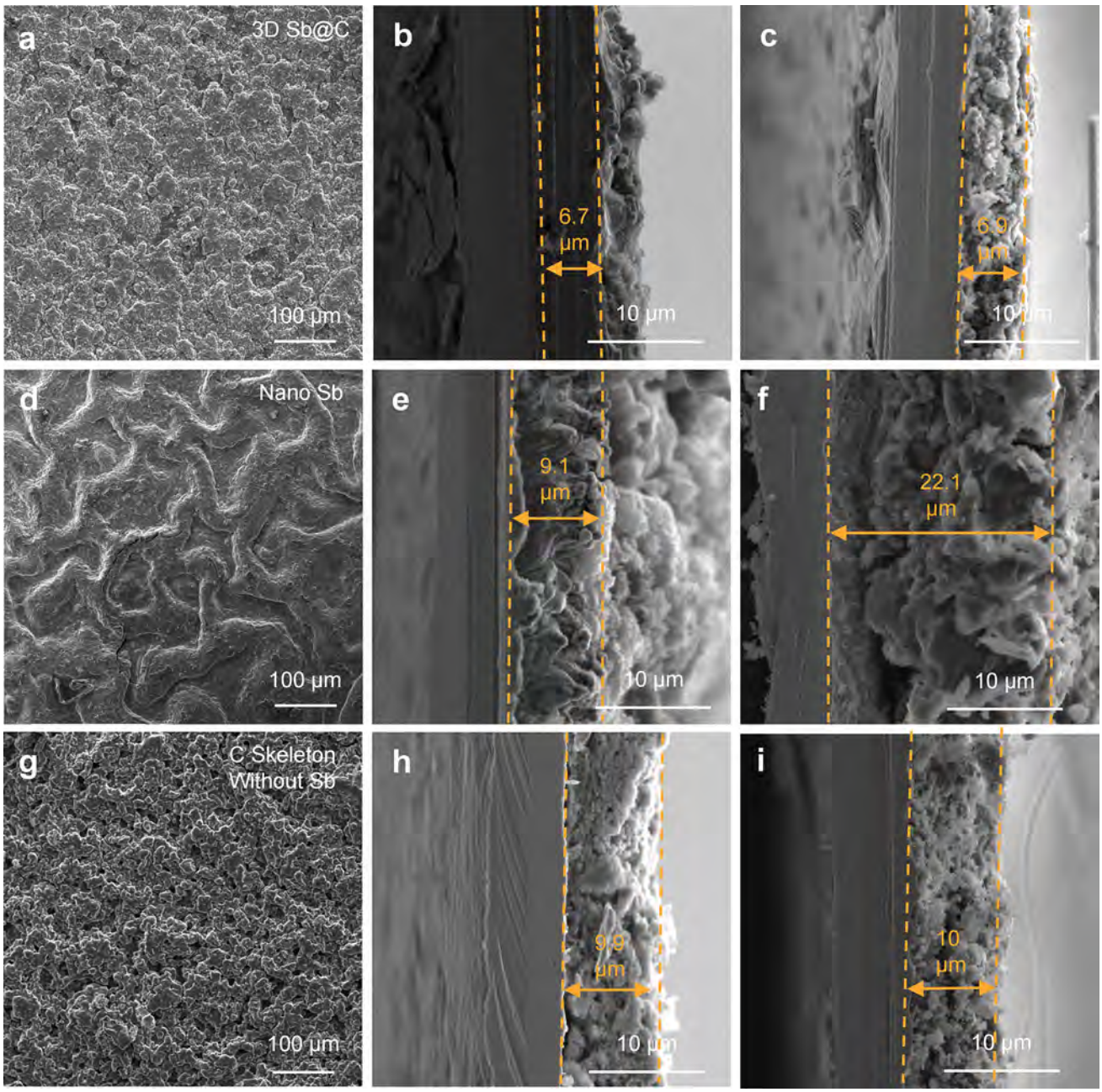

Fig. 4 Microtopography of 3D Sb@C and nano Sb electrode. Top-view SEM images of **a** 3D Sb@C, **d** nano Sb and **g** carbon skeleton without Sb; side-view images of **b**, **c** 3D Sb@C, **e**, **f** nano Sb and **h**, **i** carbon skeleton without Sb before and after first lithiation

during the lithiation–delithiation cycles [35]. The amorphous materials not only achieve rapid Li^+ diffusion by providing highly isotropic channels but also allow weak lattice distortion and limit volume change during the discharge/charge process [36].

3.5 Expanding applications of 3D Sb@C

The Sb@C composite strategy, aimed at mitigating the huge volume expansion and increasing the electronic conductivity, exhibits potential for broader applications beyond lithium-ion systems. From Fig. S15, three oxidation peaks and one oxidation peak are recognized in the CV profiles of the 3D Sb@C composite in Na-ion systems, indicating the high reversibility of the multistep transformation of Sb to Na_xSb ($x \leq 3$) [37]. Furthermore, Na^+ storage kinetics are systematically analyzed based on CV data (Fig. S16a–c). It can be found that capacitive contributes mostly to capacity, which suggests the fast electrochemical kinetics of the 3D Sb@C electrode in Na-ion

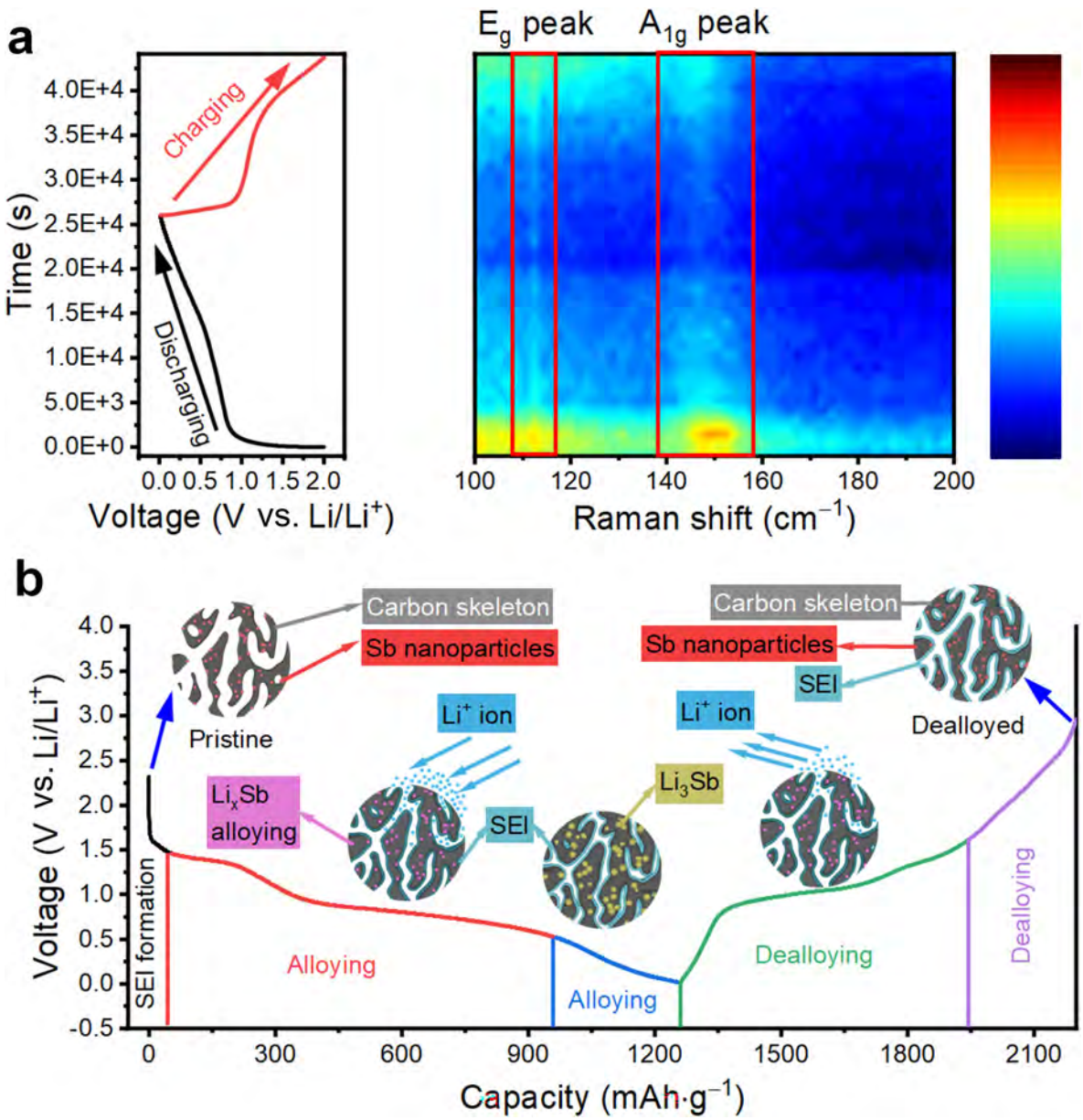

Fig. 5 Lithium storage mechanism analysis of 3D Sb@C electrode. **a** In situ Raman spectra and **b** schematic diagram of Li storage mechanism during lithiation–delithiation process

systems. Benefiting from these characteristics, the 3D Sb@C electrode can be expected to deliver appealing performances in Na-ion batteries.

3D Sb@C||Na coin-type half cells were further assembled to evaluate the electrochemical performance of the 3D Sb@C electrode in Na-ion batteries. As shown in Fig. S17, the 3D Sb@C electrode exhibits superior rate capability with reversible capacities of 320.6, 299.0, 270.7, 247.8, 224.5 and 183.3 mAh·g^{-1} at 0.1, 0.2, 0.5, 1, 2 and 5 A·g^{-1}, respectively. When the current density decreases back to 0.1 A·g^{-1}, the capacity of the 3D Sb@C electrode can recover to 308 mAh·g^{-1} and remain steady for the following cycles. Figure S18 demonstrates the cycling performance of the 3D Sb@C electrode at 1 A·g^{-1}. The 3D Sb@C electrode maintains a high reversible capacity of 230.8 mAh·g^{-1} after 500 cycles with a capacity retention of 86.15%. According to the EIS results of the 3D Sb@C electrode before and after 5, 10, 50 and 100 cycles, the R_{ct} values are almost identical, implying that a stable SEI is formed, and the 3D porous carbon framework is well maintained after repetitive alloying-dealloying (Fig. S19). The outstanding long-term cycling stability and rate performance of the 3D Sb@C electrode in Na-ion batteries can be ascribed to its 3D porous protective structure, which

can effectively accommodate the volume expansion of Sb, promote the formation of a stable SEI layer, and increase the structural integrity of the material.

4 Conclusion

The porous carbon framework inlaid evenly with nano Sb particles was successfully synthesized using a facile, cost-effective and scalable magnesiothermic reduction of $C_8H_4K_2O_{12}Sb_2$-$3H_2O$. The nanopores of porous carbon provide buffer spaces to accommodate the volume expansion of Sb during cycling. Meanwhile, the 3D interconnected carbon frameworks shorten the ion/electron transport pathway and accelerate the electrochemical kinetics of the energy storage. Moreover, the carbon skeletons isolate the Sb particles from the liquid electrolyte, avoiding the overgrowth of unstable SEIs. The high conductivity, short ion diffusion distance and excellent electrochemical stability of the 3D Sb@C composite enable the outstanding C-rate performance (5 $A{\cdot}g^{-1}$) and excellent cycling stability (> 1000 cycles). Consequently, the 3D Sb@C composite delivers an initial discharge capacity of 989 $mAh{\cdot}g^{-1}$. Significantly, the 3D Sb@C anode exhibits stable long-term cycling over 1000 cycles, with a final capacity retention of 68.7% at 5 $A{\cdot}g^{-1}$. Also importantly, employing similar design principles in Na^+ batteries, the 3D Sb@C composite has exhibited an impressive discharging capability (575 $mAh{\cdot}g^{-1}$) and a stable cycling performance (> 500 cycles, 84.8% capacity retention) as well. This strategy for the preparation of 3D porous Sb@C composite has large potential in next-generation rechargeable batteries with fast charging and ultralong life.

Acknowledgements This study was financially supported by the National Natural Science Foundation of China (No. 22309056), the National Key R&.D Program of China (No. 2022YFB2404800), the Basic Research Program of Shenzhen Municipal Science and Technology Innovation Committee (No. JCYJ20210324141613032), the Knowledge Innovation Project of Wuhan City (No. 2022010801010303), the City University of Hong Kong Strategic Research Grant (SRG), Hong Kong, China (No. 7005505), the City University of Hong Kong Donation Research Grant, Hong Kong, China (No. DON-RMG 9229021) and the Postdoctoral Fellowship Program of CPSF (No. GZB20230552).

Declarations

Conflict of interests The authors declare that they have no conflict of interest.

References

[1] Yang ZZ, Zhang CY, Ou YQ, Su ZK, Zhao Y, Cong HJ, Ai XP, Qian JF. Amorphous Sb/C composite with isotropic expansion property as an ultra-stable and high-rate anode for lithium-ion batteries. Rare Met. 2024;43(5):2039. https://doi.org/10.1007/s12598-023-02548-x.

[2] Liu X, Zhu JL, Wang XY, Yue LG, Wang W, Wang BC, Shen DJ, Li YY. Boosting potassium storage kinetics, stability, and volumetric performance of honeycomb-like porous red phosphorus via in situ embedding self-growing conductive nano--metal networks. Adv Func Mater. 2023;33(9):2209388. https://doi.org/10.1002/adfm.202209388.

[3] Zhao WQ, Zhang LM, Jiang F, Chang XH, Yang Y, Ge P, Sun W, Ji XB. Engineering metal sulfides with hierarchical interfaces for advanced sodium-ion storage systems. J Mater Chem A. 2020;8(10):5284. https://doi.org/10.1039/C9TA13899D.

[4] Zhao WQ, Yuan SH, Zhang LM, Jiang F, Yang Y, Zou GQ, Hou HS, Ge P, Sun W, Ji XB. Engineering metal-sulfides with cations-tunable metal-oxides electrocatalysts with promoted catalytic conversion for robust ions-storage capability. Energy Storage Mater. 2022;45:1183. https://doi.org/10.1016/j.ensm.2021.11.019.

[5] Liu X, Zhu JL, Yue LG, Wang XY, Wang W, Zheng TJ, Li YY. Green and scalable template-free strategy to fabricate honeycomb-like interconnected porous micro-sized layered Sb for high-performance potassium storage. Small. 2022;18(46):2204552. https://doi.org/10.1002/smll.202204552.

[6] Ge P, Zhang LM, Zhao WQ, Yang Y, Sun W, Ji XB. Interfacial bonding of metal-sulfides with double carbon for improving reversibility of advanced alkali-Ion batteries. Adv Func Mater. 2020;30(16):1910599. https://doi.org/10.1002/adfm.201910599.

[7] Zhao WQ, Lei SY, Li JX, Jiang F, Wu TJ, Yang Y, Sun W, Ji XB, Ge P. Modulating internal coordination configurations for high-density atomic antimony toward advanced fast-charging sodium-ion batteries. Adv Energy Mater. 2024;14:2304431. https://doi.org/10.1002/aenm.202304431.

[8] Liu X, Wang XY, Zhou Y, Wang B, Zhao L, Zheng H, Wang J, Liu JH, Liu J, Li YY. Novel ultra-stable 2D SbBi alloy structure with precise regulation ratio enables long-stable potassium/lithium-ion storage. Adv Mater. 2024;36(11):2308447. https://doi.org/10.1002/adma.202308447.

[9] Zhao WQ, Yuan SH, Lei SY, Zeng ZH, Dong JF, Jiang F, Yang Y, Sun W, Ji XB, Ge P. Tailoring rational crystal orientation and tunable sulfur vacancy on metal-sulfides toward advanced ultrafast ion-storage capability. Adv Func Mater. 2023;33(5):2211542. https://doi.org/10.1002/adfm.202211542.

[10] Liu ZG, Liu X, Wang BC, Wang XY, Lu DZ, Shen DJ, Sun ZF, Liu YC, Zhang WL, Zhang QB, Li YY. Ultra-thick, dense dual-encapsulated Sb anode architecture with conductively elastic networks promises potassium-ion batteries with high areal and volumetric capacities. eScience. 2023;3(6):100177. https://doi.org/10.1016/j.esci.2023.100177.

[11] Ramireddy T, Sharma N, Xing T, Chen Y, Leforestier J, Glushenkov AM. Size and composition effects in Sb-carbon nanocomposites for sodium-ion batteries. ACS Appl Mater Interfaces. 2016;8(44):30152. https://doi.org/10.1021/acsami.6b09619.

[12] Reddy JR, Ravi G, Suresh P, Veldurthi NK, Velchuri R, Vithal M. Antimony potassium tartrate. J Therm Anal Calorim. 2013;115(2):1321. https://doi.org/10.1007/s10973-013-3502-8.

[13] Jiao TF, Guo HY, Zhang QR, Peng QM, Tang YF, Yan XH, Li BB. Reduced graphene oxide-based silver nanoparticle-containing composite hydrogel as highly efficient dye catalysts for wastewater treatment. Sci Rep. 2015;5(1):11873. https://doi.org/10.1038/srep11873.

[14] Li C, Zhang X, Wang K, Sun XZ, Liu GH, Li JT, Tian HF, Li JQ, Ma YW. Scalable self-propagating high-temperature synthesis of graphene for supercapacitors with superior power

density and cyclic stability. Adv Mater. 2017;29(7):1604690. https://doi.org/10.1002/adma.201604690.
[15] Hou HS, Jing MJ, Yang YC, Zhang Y, Zhu YR, Song WX, Yang XM, Ji XB. Sb porous hollow microspheres as advanced anode materials for sodium-ion batteries. J Mater Chem A. 2015;3(6): 2971. https://doi.org/10.1039/c4ta06476c.
[16] Liu ZM, Yu X-Y, Lou XW, Paik U. Sb@C coaxial nanotubes as a superior long-life and high-rate anode for sodium ion batteries. Energy Environ Sci. 2016;9(7):2314. https://doi.org/10.1039/c6ee01501h.
[17] Yang XM, Wang JK, Wang S, Wang HK, Tomanec O, Zhi CY, Zboril R, Yu DYW, Rogach A. Vapor-infiltration approach toward selenium/reduced graphene oxide composites enabling stable and high-capacity sodium storage. ACS Nano. 2018; 12(7):7397. https://doi.org/10.1021/acsnano.8b04114.
[18] Verma R, Singhbabu YN, Didwal PN, Nguyen AG, Kim J, Park CJ. Biowaste orange peel-derived mesoporous carbon as a cost-effective anode material with ultra-stable cyclability for potassium-ion batteries. Batteries Supercaps. 2020;3(10):1099. https://doi.org/10.1002/batt.202000068.
[19] Liang K, Ren Y-R. Stabilization of Sb nanoparticles using metal-organic frameworks to obtain stable performance of anode material for sodium-ion batteries. Rare Met. 2022;41(5):1406. https://doi.org/10.1007/s12598-021-01924-9.
[20] Cui CY, Xu JT, Zhang YQ, Wei ZX, Mao ML, Lian X, Wang SY, Yang CY, Fan XL, Ma JM, Wang CS. Antimony nanorod encapsulated in cross-linked carbon for high-performance sodium ion battery Anodes. Nano Lett. 2018;19(1):538. https://doi.org/10.1021/acs.nanolett.8b04468.
[21] Le HTT, Pham XM, Park CJ. Facile citrate gel synthesis of an antimony-carbon nanosponge with enhanced lithium storage. New J Chem. 2019;43(27):10716. https://doi.org/10.1039/c9nj00762h.
[22] Jing WT, Zhang Y, Gu Y, Zhu YF, Yang CC, Jiang Q. N-doped carbon nanonecklaces with encapsulated Sb as a sodium-ion battery anode. Matter. 2019;1(3):720. https://doi.org/10.1016/j.matt.2019.03.010.
[23] Wang GY, Zhu M, Zhang Y, Song C, Zhu XL, Huang ZY, Zhang YJ, Yu FF, Xu G, Wu MH, Liu HK, Dou SX, Wu C. Double interface regulation: toward highly stable lithium metal anode with high utilization. InfoMat. 2022;4(7): e12293. https://doi.org/10.1002/inf2.12293.
[24] Gong DC, Wei CY, Xie DH, Tang YB. Ultrasmall antimony nanodots embedded in carbon nanowires with three-dimensional porous structure for high-performance potassium dual-ion batteries. Chem Eng J. 2022;431:133444. https://doi.org/10.1016/j.cej.2021.133444.
[25] Yu WQ, Zhu CY, Wang RT, Chen JC, Liu QY, Zhang SX, Gao ZJ, Wang CX, Zhang ZW, Yin LW. Advanced sodium-ion capacitor based on antimony-carbon composite anode. Rare Met. 2022;41(10):3360. https://doi.org/10.1007/s12598-022-02015-z.
[26] Gu Y, Xi BJ, Zhang H, Ma YC, Xiong SL. Activation of main-group antimony atomic sites for oxygen reduction catalysis. Angew Chem Int Ed. 2022;61(26): e202202200. https://doi.org/10.1002/anie.202202200.
[27] Peng PP, Wu YR, Li XZ, Zhang JH, Li YW, Cui P, Yi TF. Toward superior lithium/sodium storage performance: design and construction of novel TiO_2-based anode materials. Rare Met. 2021;40(11):3049. https://doi.org/10.1007/s12598-021-01742-z.
[28] Pan SY, Han JW, Wang YQ, Li ZS, Chen FQ, Guo Y, Han ZS, Xiao KF, Yu ZC, Yu MY, Wu SC, Wang D-W, Yang QH. Integrating SEI into layered conductive polymer coatings for ultrastable silicon anodes. Adv Mater. 2022;34(31):2203617. https://doi.org/10.1002/adma.202203617.
[29] Wang FX, Xie JH, Zheng DZ, Yang F, Zhang HZ, Lu XH. Intrinsic carbon defects induced reversible antimony chemistry for high-energy aqueous alkaline batteries. Adv Mater. 2022; 34(17):2200085. https://doi.org/10.1002/adma.202200085.
[30] Lin X-P, Xue FF, Zhang ZG, Li QH. Sb nanoparticles encapsulated in N-doped carbon nanotubes as freestanding anodes for high-performance lithium and potassium ion batteries. Rare Met. 2022;42(2):449. https://doi.org/10.1007/s12598-022-02143-6.
[31] Yao TH, Wang HK, Qin YB, Shi JW, Cheng YH. Enhancing pseudocapacitive behavior of MOF-derived TiO_{2-x}@Carbon nanocubes via Mo-doping for high-performance sodium-ion capacitors. Compos B Eng. 2023;253: 110557. https://doi.org/10.1016/j.compositesb.2023.110557.
[32] Yao TH, Wang HK, Ji X, Zhang QM, Meng LJ, Cheng YH, Chen Y, Han XG. Encapsulation of titanium disulfide into MOF-derived N,S-doped carbon nanotablets toward suppressed shuttle effect and enhanced sodium storage performance. Small. 2024;2311126. https://doi.org/10.1002/smll.202311126.
[33] Yang L, Liu ML, Xiang YE, Deng WT, Zou GQ, Hou HS, Ji XB. Carbon skeleton confined Sb chalcogenides nanodots for stable sodium storage. Carbon. 2022;197:341. https://doi.org/10.1016/j.carbon.2022.06.043.
[34] Xiao B, Wu G, Wang TD, Wei ZG, Sui YW, Shen BL, Qi JQ, Wei FX, Meng QK, Ren YJ, Xue XL, Zheng JC, Mao J, Dai KH, Yan Q. Tin antimony oxide @graphene as a novel anode material for lithium ion batteries. Ceram Int. 2022;48(2):2118. https://doi.org/10.1016/j.ceramint.2021.09.300.
[35] Yuan YT, Jan S, Wang ZY, Jin XB. A simple synthesis of nanoporous Sb/C with high Sb content and dispersity as an advanced anode for sodium ion batteries. J Mater Chem A. 2018;6(14):5555. https://doi.org/10.1039/c8ta00592c.
[36] Xu X, Si L, Zhou XS, Tu FZ, Zhu XS, Bao JC. Chemical bonding between antimony and ionic liquid-derived nitrogen-doped carbon for sodium-ion battery anode. J Power Sources. 2017;349:37. https://doi.org/10.1016/j.jpowsour.2017.03.026.
[37] Darwiche A, Marino C, Sougrati MT, Fraisse B, Stievano L, Monconduit L. Better cycling performances of bulk Sb in Na-ion batteries compared to Li-ion systems: an unexpected electrochemical mechanism. J Am Chem Soc. 2012;134(51):20805. https://doi.org/10.1021/ja310347x.

Springer

RARE METALS

Supporting Information

Antimony nanoparticles encapsulated in three-dimensional porous carbon frameworks for high-performance rechargeable batteries

An-Qi Chen, Si-Guang Guo, Yu Liu*, Ling Long, Zhuo Li*, Biao Gao, Paul K. Chu, Kai-fu Huo

A.-Q Chen, S.-G Guo, Y. Liu*, Z. Li*, B. Gao

The State Key Laboratory of Refractories and Metallurgy and Institute of Advanced Materials and Nanotechnology, Wuhan University of Science and Technology, 430081, Wuhan, China

e-mail: zhuo_li@wust.edu.cn; liyu_lab@163.com

L. Long

Hubei Huazhong Electric Power Technology Development Co., Ltd. Huazhong Electric Power Technology Building, No. 236 Zhongbei Road, Wuhan, China

B. Gao, Paul K. Chu

Department of Physics and Department of Materials Science and Engineering, City University of Hong Kong, Tat Chee Avenue, Kowloon 999077 Hong Kong, China

A K.-F Huo

Wuhan National Laboratory for Optoelectronics (WNLO), Huazhong University of Science and Technology, 430074, Wuhan, China

(A.-Q. Chen and S.-G Guo contributed equally to this work.)

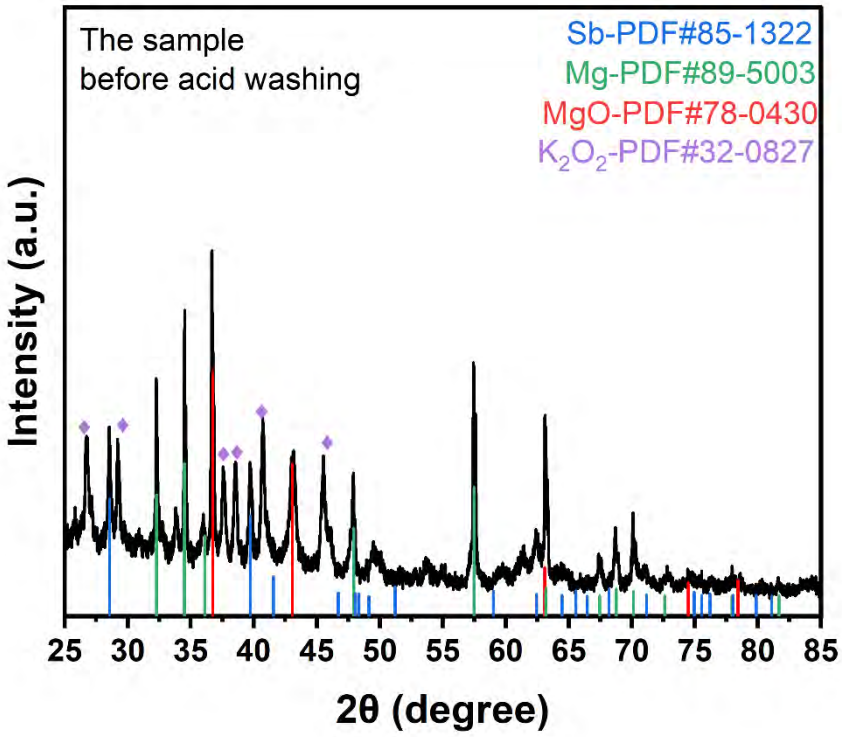

Fig. S1. The XRD spectra of the samples after and before acid washing

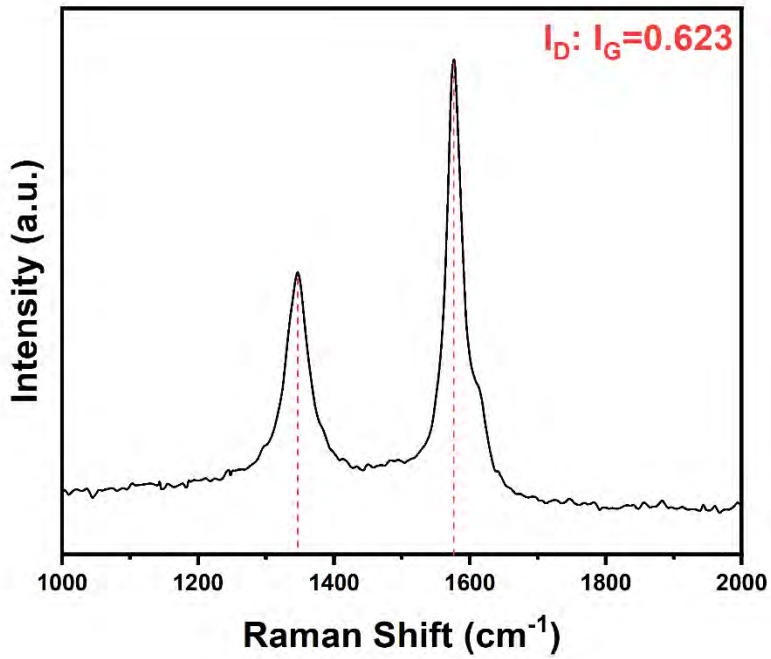

Fig. S2. The Raman spectra of the sample before acid washing

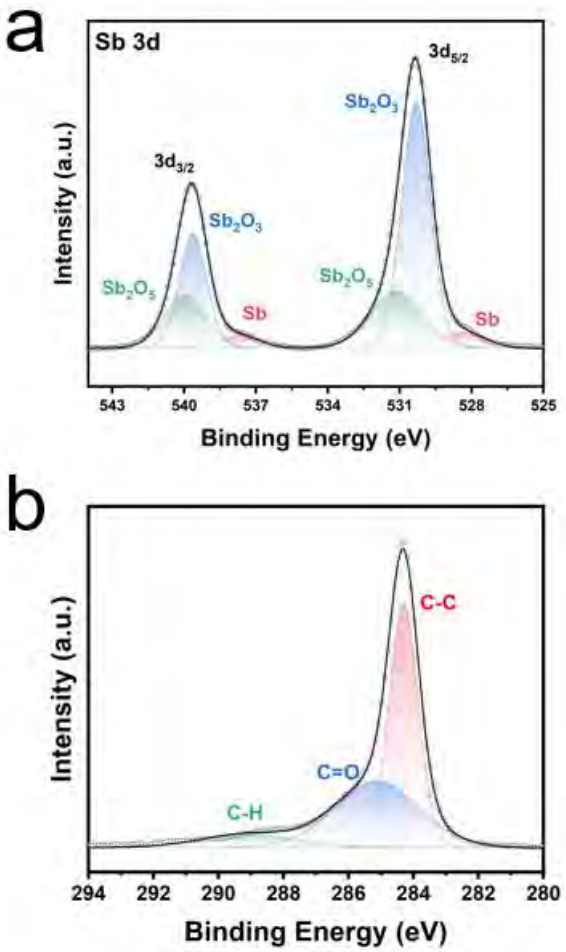

Fig. S3. The XPS spectrum of 3D Sb@C

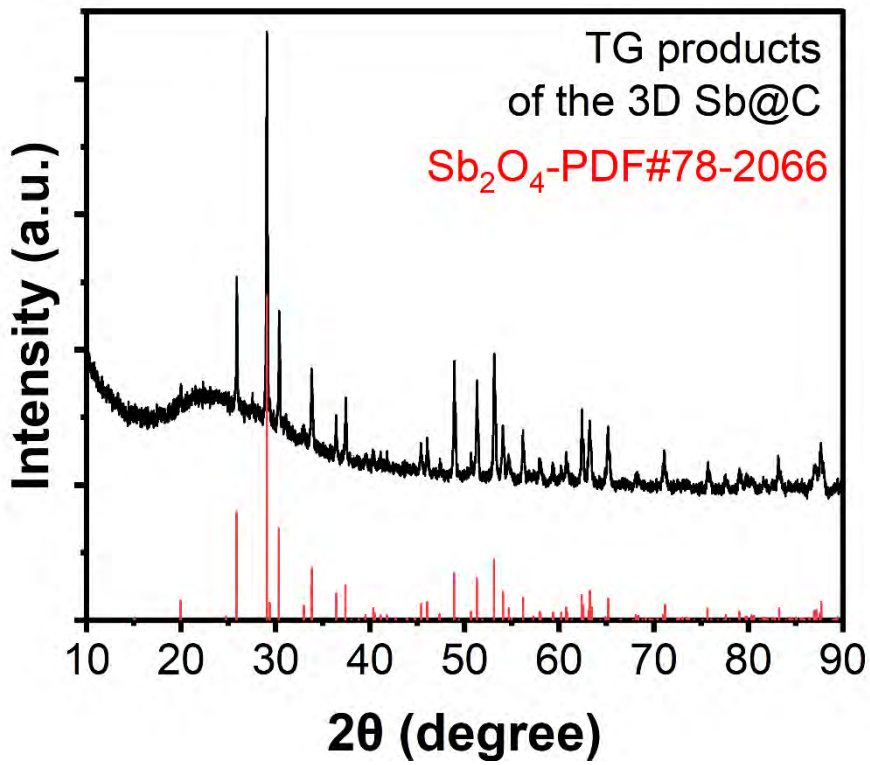

Fig. S4. XRD spectra of the residue after heating from the room temperature to 800 °C with a heating rate of 5 °C/min in an air atmosphere.

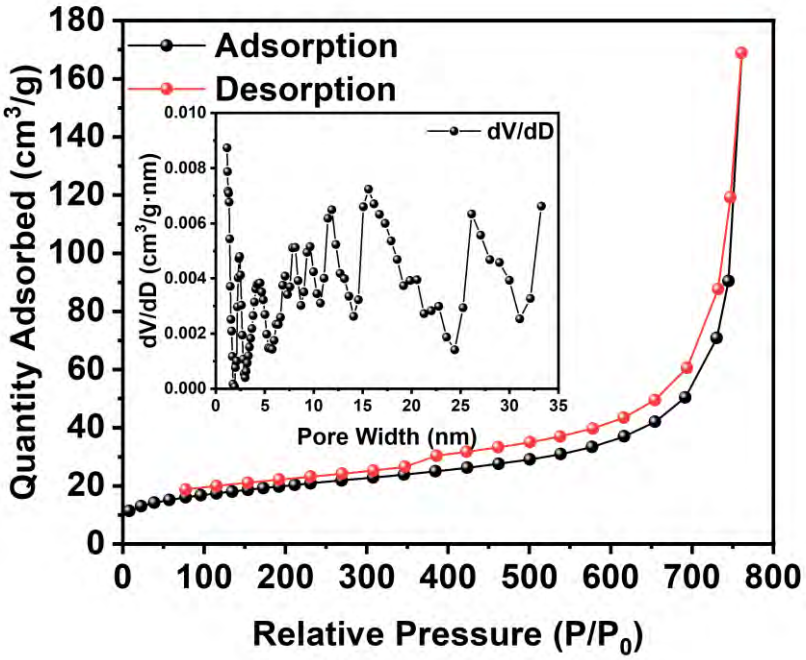

Fig. S5. Brunauer–Emmett–Telle (BET) results: Nitrogen adsorption-desorption curves, inset is the pore size distributions

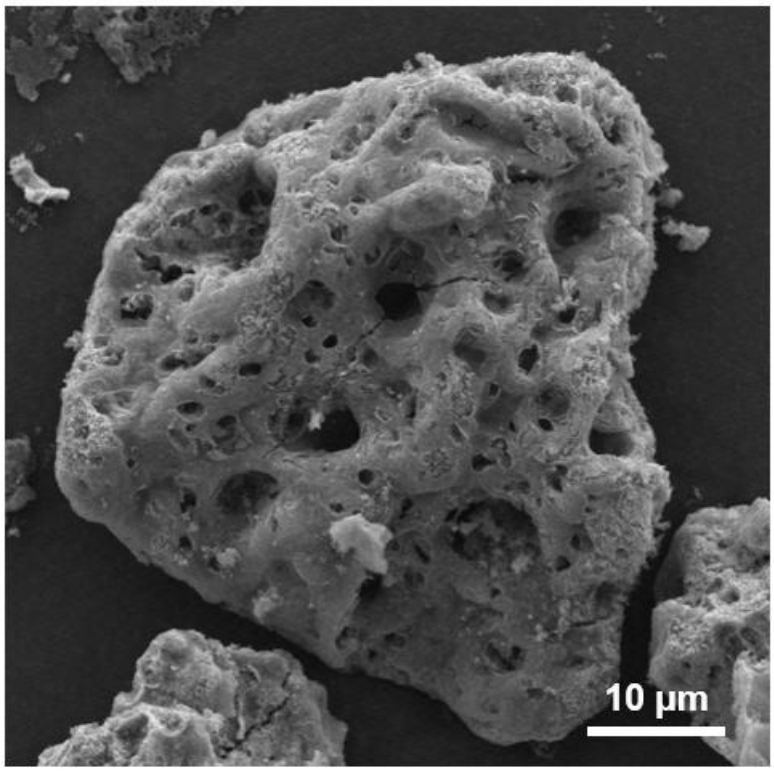

Fig. S6. Surface SEM image of the 3D Sb@C

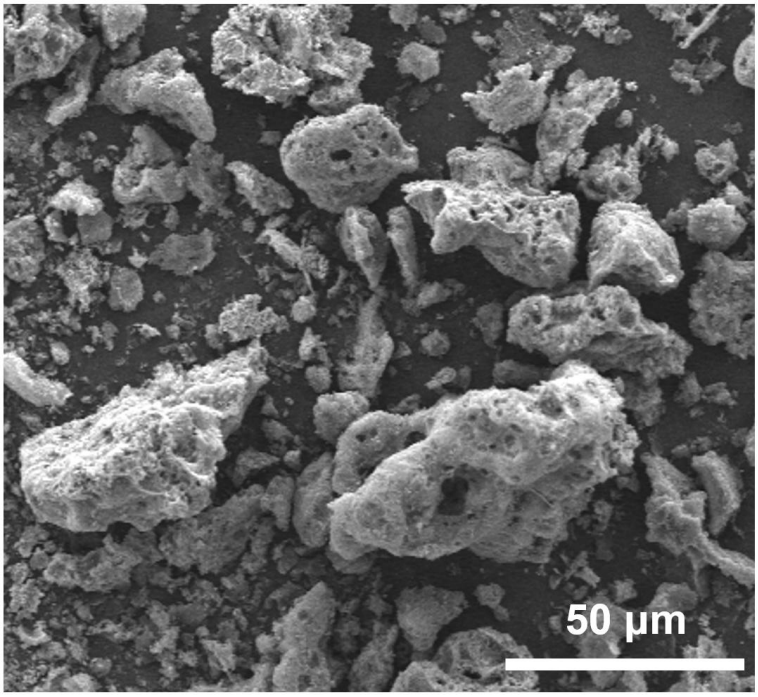

Fig. S7. SEM image of the 3D Sb@C with a magnification of 1500×

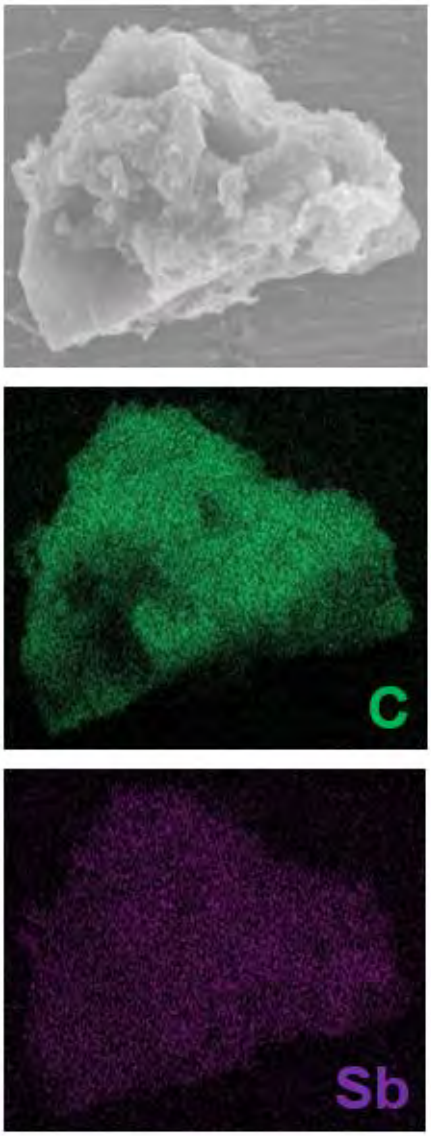

Fig. S8. The EDS mapping of 3D Sb@C based on SEM

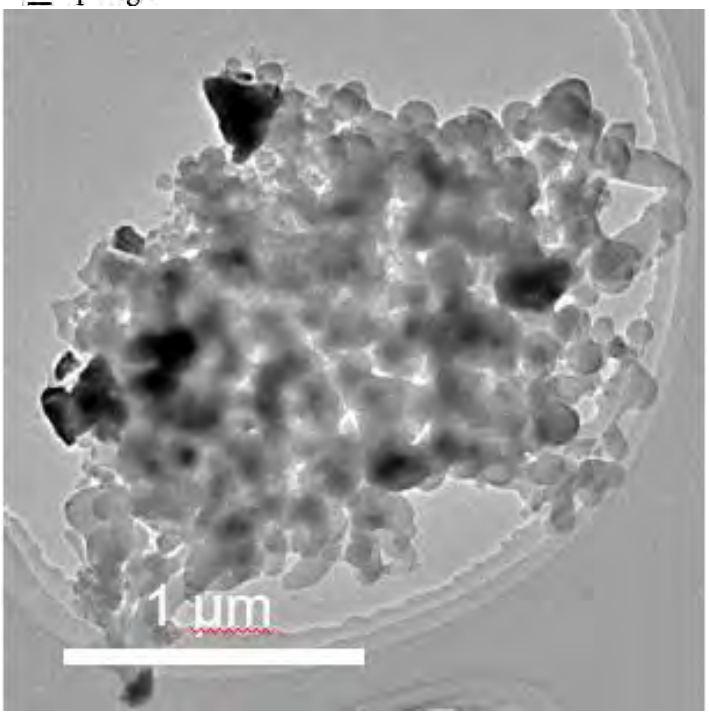

Fig. S9. The TEM image of 3D Sb@C

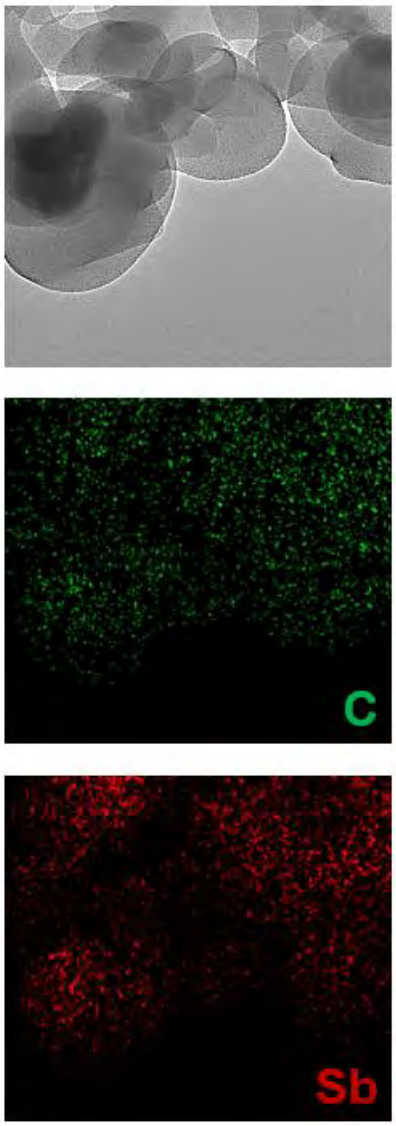

Fig.S10. The EDS mapping of 3D Sb@C based on TEM

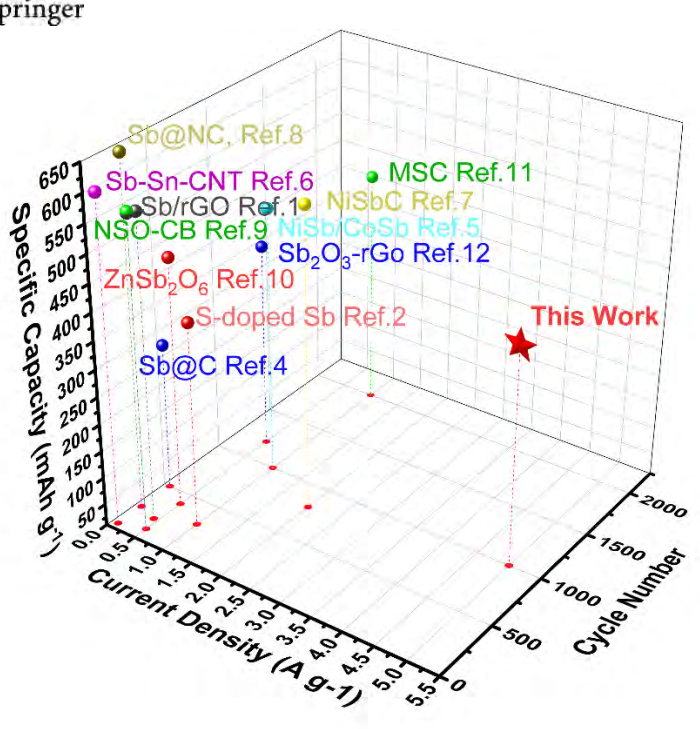

Fig. S11. Comparison of the cell performance of Sb based anodes in this work with other reports.[1-12]

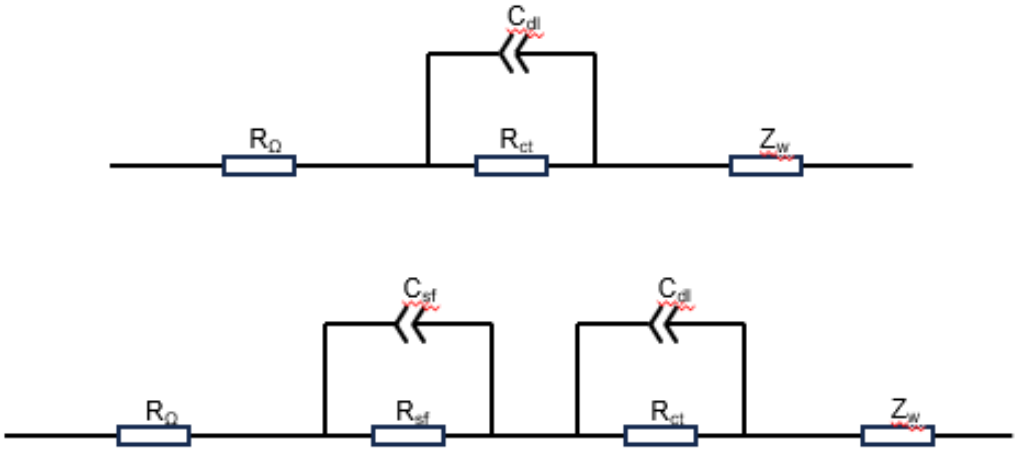

Fig. S12. The figure shows an analog circuit diagram for electrochemical impedance testing. a) before cycling. b) after cycling

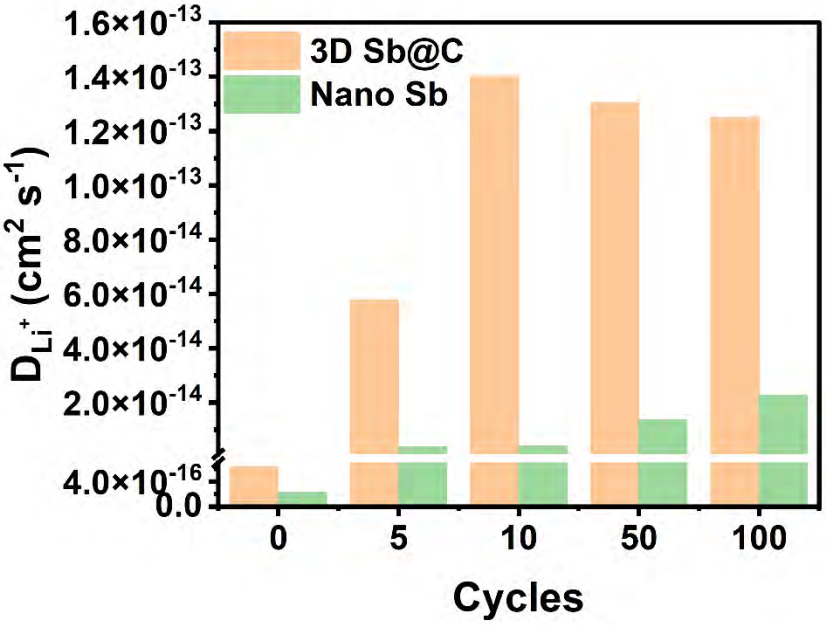

Fig. S13. Lithium-ion diffusion coefficient of the 3D Sb@C electrolyte calculated based on EIS plots

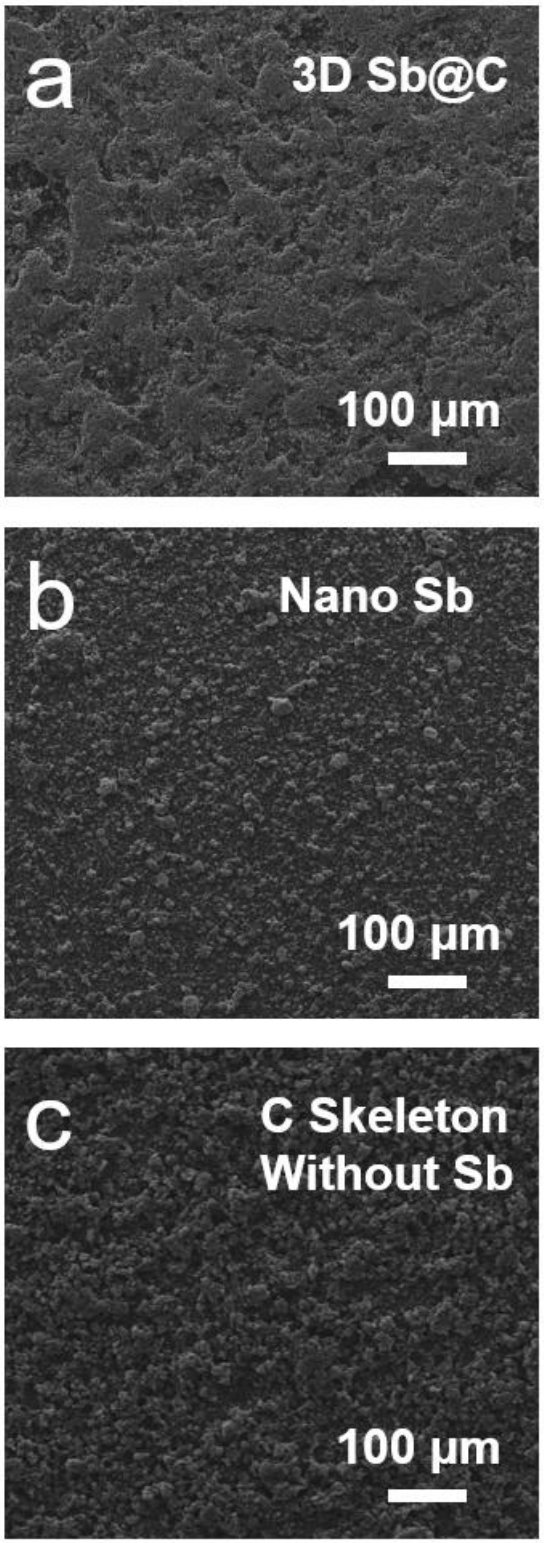

Fig. S14. SEM images of different electrodes before cycling. (a) 3D Sb@C, (b) Nano Sb, (c) 3D C skeleton without Sb.

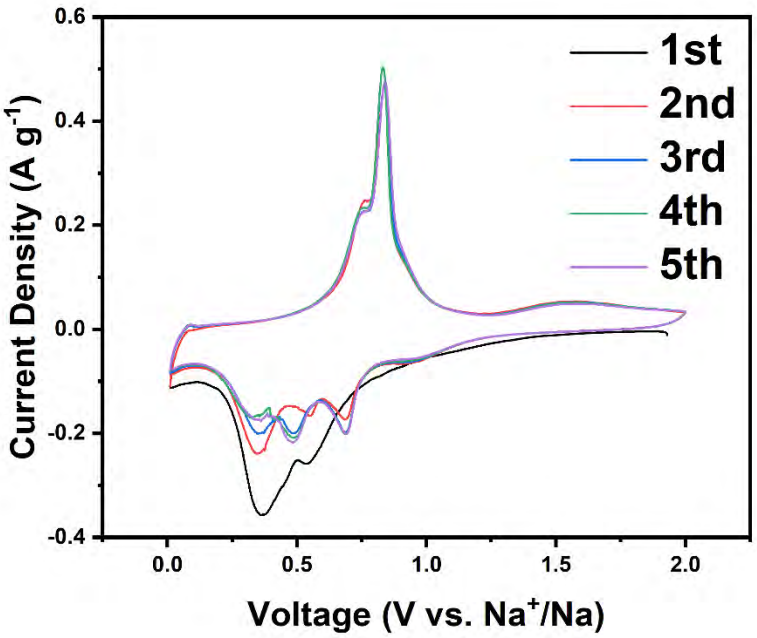

Fig. S15. A CV curve of 3D Sb@C electrodes in Na ion batteries for 5 cycles at 0.1 mV s-1 in a potential range of 0.01-2.00 V vs. Na+/Na.

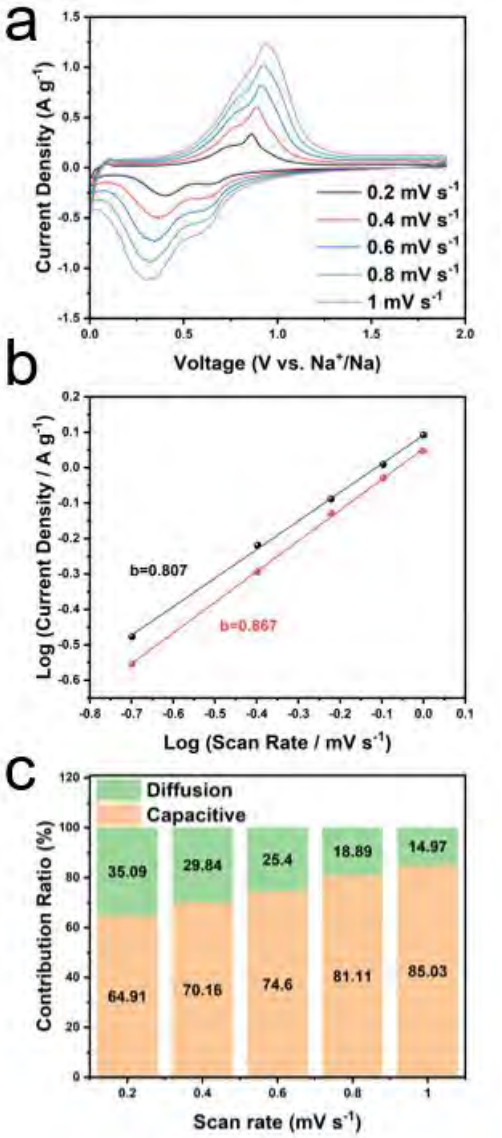

Fig. S16. Diffusion kinetic analysis of 3D Sb@C in a Na-ion battery. a) CV curves of 3D Sb@C electrode at different scan rates. b) Logarithmic peak current vs. scan rate relationship. c) Contribution ratio of diffusion-controlled and capacitance.

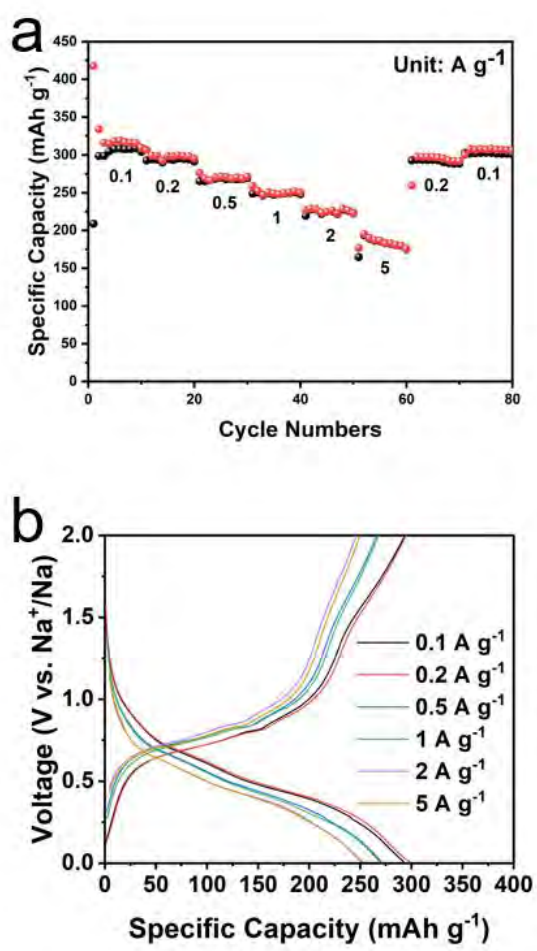

Fig. S17. a) The rate performance test of 3D Sb@C electrodes in Na ion batteries. b) The GCD curve at different current densities of 3D Sb@C electrodes in Na ion batteries.

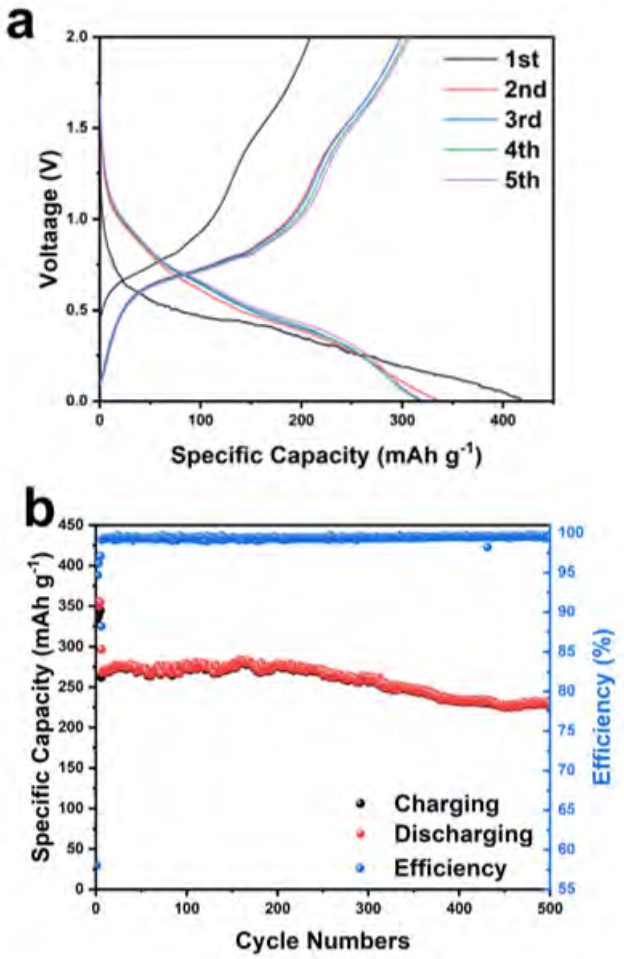

Fig. S18. a) The GCD curve of 3D Sb@C electrodes in Na ion batteries for 5 cycles. b) The excellent long-term performance.

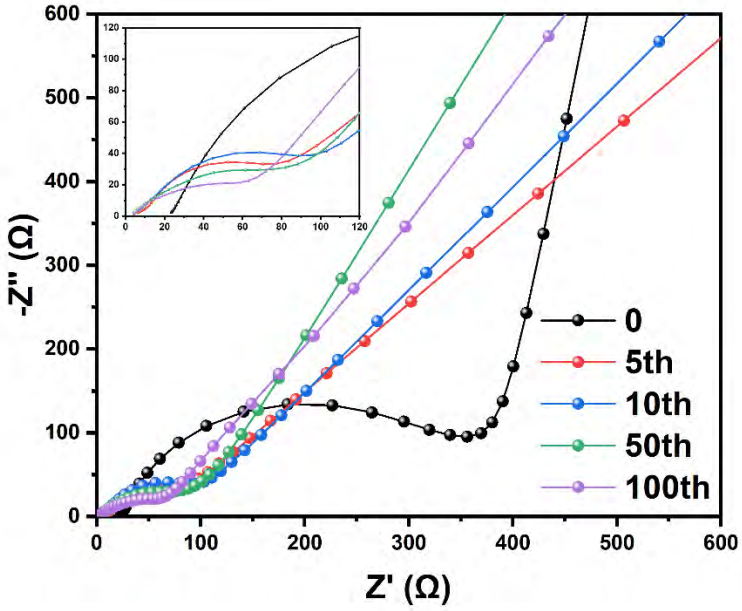

Fig. S19. The Nyquist plots of the 3D Sb@C in a Na-ion battery at different cycles

Table. S1. Comparison of the cell performance of Sb based anodes in this work with other reports. [1-12]

Ref.	Materials/ Details	Synthesis Method	Initial Charge Capacity (mAh g^{-1}) with ICE	Rate Capacity (mAh g^{-1} / A g^{-1})	Cycle Stability (mAh g^{-1} / cycles / A g^{-1})
1	Antimony/reduced graphene oxide (Sb/rGO) composite	a facile one-step chemical deposition route	1214 mAh g^{-1} with 52.8%	210 mAh g^{-1} at 2 A g^{-1}	563 mAh g^{-1} after 200 cycles at 0.43 A g^{-1}
2	S-doped Sb/Sb_2O_3/CNT/GNR nanocomposite	the one-step hydrothermal synthesis	984 mAh g^{-1} with 62.5%	328 mAh g^{-1} at 2 A g^{-1}	383 mAh g^{-1} after 300 cycles at 1 A g^{-1}
3	3.75 M LiFSI/0.5 M LiDFOB	electrolyte design	668 mAh g^{-1} with 85.2%	525 mAh g^{-1} at 5 A g^{-1}	576 mAh g^{-1} after 100 at 0.5 A g^{-1}
4	microspherical Sb@C	Pyrolytic reduction of organic materials	721 mAh g^{-1} with 63.5%	336 mAh g^{-1} at 0.5 A g^{-1}	280 mAh g^{-1} after 500 cycles at 0.1 A g^{-1}
5	NiSb/CoSb nanoparticles embedded in carbon nanosphere	template sacrifice method	518 mAh g^{-1} with 48.6%	352 mAh g^{-1} at 1 A g^{-1}	495 mAh g^{-1} after1000 at 1 A g^{-1}
6	Sb-Sn-CNT nanocomposite	galvanostatic electrodeposition	606 mAh g^{-1} with 97%	545 mAh g^{-1} at 1 A g^{-1}	600 mAh g^{-1} after 50 cycles at 0.1 A g^{-1}
7	NiSbC	template and substitution reactions	1004 mAh g^{-1} with 56.9%	467 mAh g^{-1} at 4 A g^{-1}	559 mAh g^{-1} after 800 cycles at 2 A g^{-1}
8	Sb nanoparticles encapsulated in N-doped carbon nanotubes	electrospinning method	756 mAh g^{-1} with 75.4%	220 mAh g^{-1} at 10 A g^{-1}	643 mAh g^{-1} after 250 cycles at 0.1 A g^{-1}
9	nickel antimony oxide-carbon black (NSO-CB)	co-precipitation method	822 mAh g^{-1} with 60.5%	348 mAh g^{-1} at 6 A g^{-1}	574 mAh g^{-1} after 100 cycles at 0.5 A g^{-1}
10	Zinc antimony oxide ($ZnSb_2O_6$)	Electrophoretic Deposition	600 mAh g^{-1} with 99.5%	370 mAh g^{-1} at 4 A g^{-1}	464 mAh g^{-1} after 400 cycles at 0.5 A g^{-1}
11	MXene-reinforced Sb@C (MSC) nanocomposite	in-situ growing Sb-MOF over the conductive MXene	625 mAh g^{-1} with 72.1%	305 mAh g^{-1} at 10 A g^{-1}	439 mAh g^{-1} after 2000 cycles at 1 A g^{-1}
12	Octahedral Sb_2O_3-rGO	hydrothermal method	645 mAh g^{-1} with 57.2%	208 mAh g^{-1} at 5 A g^{-1}	386 mAh g^{-1} after 1200 cycles at 0.5 A g^{-1}
This Work	3D Sb@C	one-step low temperature MR	735 mAh g^{-1} with 74%	437 mAh g^{-1} at 5 A g^{-1}	410 mAh g^{-1} after 1000 cycles at 5 A g^{-1}

Springer

Table S2. Fitting results of the Nyquist plots of the electrodes after cycling in a Li-ion battery.

Sample	Pristine			5 cycles			10 cycles			50 cycles			100 cycles		
	R_Ω (Ω)	R_{sf} (Ω)	R_{ct} (Ω)	R_Ω (Ω)	R_{sf} (Ω)	R_{ct} (Ω)	R_Ω (Ω)	R_{sf} (Ω)	R_{ct} (Ω)	R_Ω (Ω)	R_{sf} (Ω)	R_{ct} (Ω)	R_Ω (Ω)	R_{sf} (Ω)	R_{ct} (Ω)
3D Sb@C	1.475		41.56	1.501	1.26	27.32	1.458	2.193	20.81	1.388	2.69	17.59	1.444	4.12	11.01
Nano Sb	2.369		134	2.593	3.719	21.48	2.365	4.703	25.23	2.382	5.549	29.469	2.397	8.166	31.79

Reference

[1] Sun Q, Cao Z, Ma Z, Zhang J, Wahyudi W, Cai T, Cheng H, Li Q, Kim H, Xie E, Cavallo L, Sun Y-K, Ming J. Discerning Roles of Interfacial Model and Solid Electrolyte Interphase Layer for Stabilizing Antimony Anode in Lithium-Ion Batteries. ACS Materials Letters. 2022;4(11):2233-2243. https://doi.org/10.1021/acsmaterialslett.2c00679.
[2] Elias L, Bhar M, Ghosh S, Martha S K. Effect of alloying on the electrochemical performance of Sb and Sn deposits as an anode material for lithium-ion and sodium-ion batteries. Ionics. 2022;28(6):2759-2768. https://doi.org/10.1007/s11581-022-04539-x.
[3] Ray U, Das D, Jena S, Mitra A, Das K, Majumder S B, Das S. Electrochemical characteristics of electrophoretically deposited nickel antimony oxide anode for lithium-ion rechargeable cells. Journal of Power Sources. 2024;594:234044. https://doi.org/10.1016/j.jpowsour.2023.234044.
[4] Ray U, Das D, Mitra A, Majumder S B, Das S. Electrochemical performance of electrophoretically deposited zinc antimony oxide–carbon black anode for lithium-ion batteries. Materials Letters. 2024;355:135567. https://doi.org/10.1016/j.matlet.2023.135567.
[5] Jaramillo-Quintero O A, Benítez-Cruz M, García-Ocampo J L, Cano A, Rincón M E. Enhanced performance of S-doped Sb/Sb2O3/CNT/GNR nanocomposite as anode material in lithium-ion batteries. Journal of Alloys and Compounds. 2019;807:151647. https://doi.org/10.1016/j.jallcom.2019.151647.
[6] Yin W, Chai W, Wang K, Ye W, Rui Y, Tang B. Facile synthesis of Sb nanoparticles anchored on reduced graphene oxides as excellent anode materials for lithium-ion batteries. Journal of Alloys and Compounds. 2019;797:1249-1257. https://doi.org/10.1016/j.jallcom.2019.04.329.
[7] Tian J, Yang H, Fu C, Sun M, Wang L, Liu T. In-situ synthesis of microspherical Sb@C composite anode with high tap density for lithium/sodium-ion batteries. Composites Communications. 2020;17:177-181. https://doi.org/10.1016/j.coco.2019.12.005.
[8] Feng L, Chen J, Li Y, Zhou S, Soomro R A, Zhang P, Xu B. MXene-reinforced Sb@C nanocomposites with synergizing spatial confinement architecture enabled ultra-stable and fast lithium ion storage. Chemical Engineering Journal. 2024;489:151396. https://doi.org/10.1016/j.cej.2024.151396.
[9] Weng C, Huang S, Lu T, Li J, Li J, Li J, Pan L. NiM (Sb, Sn)/N-doped hollow carbon tube as high-rate and high-capacity anode for lithium-ion batteries. Journal of Colloid and Interface Science. 2023;652:208-217. https://doi.org/10.1016/j.jcis.2023.08.086.
[10] Wang L, Zhu L, Zhang W, Ding G, Yang G, Xie L, Cao X. Revealing the unique process of alloying reaction in Ni-Co-Sb/C nanosphere anode for high-performance lithium storage. Journal of Colloid and Interface Science. 2021;586:730-740. https://doi.org/10.1016/j.jcis.2020.10.142.
[11] Lin X-P, Xue F-F, Zhang Z-G, Li Q-H. Sb nanoparticles encapsulated in N-doped carbon nanotubes as freestanding anodes for high-performance lithium and potassium ion batteries. Rare Metals. 2022;42(2):449-458. https://doi.org/10.1007/s12598-022-02143-6.
[12] Jin Y, Hwang H, Seong H, Moon J H, Kim G, Yoo H, Jung T, Lee J B, Choi J. Synthesis and Electrochemical Properties of Octahedral Sb2O3-rGO as Anode Materials for Lithium-Ion Batteries. ACS Applied Energy Materials. 2024;7(7):2955-2962. https://doi.org/10.1021/acsaem.4c00237.